



Finite element analysis of thermo-mechanical behavior of a multi-layer laser additive manufacturing process

Khalil Khanafer^{1,2} · Bader Alshuraiaan³ · Ali Al-Masri⁴ · Shashi Aithal⁵ · Ibrahim Deiab⁶

Received: 16 February 2021 / Accepted: 6 May 2022 / Published online: 1 June 2022
© The Author(s), under exclusive licence to Springer-Verlag France SAS, part of Springer Nature 2022

Abstract

Finite element analysis was utilized in this investigation to study the effect of varying the direction of the laser scan on the thermo-mechanical behavior of a multi-layer additive manufacturing (AM) process. The effect of varying the direction of laser rastering on the temperature distribution, strain, stress and deformation was analyzed in this study. Two laser rastering strategies were considered, namely, (a) counter-clockwise (CCW) for each of the layers deposited and, (b) alternating (CCW followed by clockwise) for each successive layer using a well-validated model. The results showed that for the geometrical configuration under consideration in this study, thermal strains were not significantly impacted by the rastering direction of the laser (CCW is lower than alternating by 8–9%). However, altering the direction of rastering leads to a 45–75% reduction in the deformation values as compared to the CCW mode. This co-relates well with the 10% difference in the maximum thermal gradient of the alternating case compared to the CCW case. The von Mises stress was found to be higher in the CCW mode as compared to the alternating mode. The findings of this investigation illustrated that the location of maximum shear stress depended on the direction of the laser rastering and followed the same trend observed in the thermal strain and the normal von Mises stress. Hence, the CCW mode was found to exhibit higher shear stresses compared with the alternating mode. This study clearly shows that the rastering direction of the laser beam has a profound effect on the thermo-mechanical behavior of the parts manufactured using AM processes.

Keywords Additive manufacturing · Deformation · Numerical simulation · Residual stresses · Scan direction · Thermal strain

1 Introduction

Additive manufacturing is receiving great attention by many researchers in the literature due to its importance in many

engineering and industrial applications. Such applications include aerospace, automotive, medical, dental, architecture, furniture and jewelry, biomedical, and oil and gas industry [1–4]. The number of applications of this technology is expanding rapidly, from small manufacturing niche products to large companies and enterprises manufacturing a wide range of products. Additive manufacturing substantially reduces materials waste, simplifies the manufacturing process, and enables the building of complex components which are difficult to build using traditional manufacturing processes.

While significant strides were made in the additive manufacturing process, there are still several problems that limit their range of applications and throughput. Thermal stresses and their impact on the microstructure imperfections are the among the main problems facing the industry. Thermal history of the additive manufacturing process also impacts “property scatter” thus affecting the consistent reproducibility of product quality. Given the importance of the thermal phenomena on the AM process, several studies

✉ Khalil Khanafer
khanafer@umich.edu

¹ Mechanical Engineering Department, University of Michigan, Flint, MI 48502, USA

² Mechanical Engineering Department, Australian University, Safat 13015, Kuwait

³ Mechanical Engineering Department, College of Engineering and Petroleum, Kuwait University, 13060 Safat, Kuwait

⁴ FEV Powertrain Technology Co. Ltd, Yanjiao, Sanhe City 065201, China

⁵ Computational Science Division, Argonne National Laboratory, 9700 S. Cass Avenue, Argonne, IL 60439, USA

⁶ Manufacturing Lab (AML), School of Engineering, University of Guelph, Guelph, ON N1G2W1, Canada

have been conducted in the literature to better understand the thermal processes during the additive manufacturing. A three-dimensional thermal model of the powder-bed fusion process of Ti–6Al–4V alloy was developed by Karayagiz et al. [5]. The model was validated using an experimental setup, with comparisons being made for size and morphology of the Heat-Affected Zone (HAZ), melt pool size and thermal history. This work utilizes dual wavelength pyrometry to validate multi-track thermal history, as opposed to single-track measurements. The authors then conducted a sensitivity analysis to determine which parameters have the most effect on the model's predictions of melt pool/HAZ size, geometry, and molten pool temperature.

Thermal conductivity of the liquid phase of the alloy, porosity of the powder bed, and radiative absorptivity were found to be the most influential parameters. Another study by Xhao et al. [6] investigated the same process, using a three-dimensional model for a single-layer process and a two-dimensional model for a multilayer process. Recently, Khanafer et al. [7] investigated numerically using finite element method transient heat transfer process during additive manufacturing process of a half cylinder for various pertinent parameters such as the speed and direction of the laser scan as well as phase change of the molten. The results presented by the authors illustrated that the travel speed and direction of the laser beam had a profound effect on the temperature variation within the manufactured part.

The high temperature gradients experienced during laser additive manufacturing may introduce significant residual stresses which can result in cracks and deformation along with non-homogeneity in the material properties and/or defects (cracks) in the manufactured parts [8–12]. Alleviating these stresses is essential to improve the quality of the built parts. Wu et al. [11] conducted an experimental study to analyze induced residual stresses in 316L stainless steel L-shaped bar for various parameters such as laser intensity and speed, scanning strategy, and build orientation. The experimental results presented by the authors showed that the residual stresses can be reduced by decreasing scan island size and increasing laser power/speed ratio.

A thermo-structural model of the powder-bed process was developed by Conti et al. [13]. This model was used to conduct a sensitivity analysis to discern the model's sensitivity to variations in material properties. Such a sensitivity study would enable researchers to focus their measurement efforts on the most crucial properties. The investigated properties were the thermal conductivity, specific heat capacity, and Young's modulus. For thermal predictions, it was found that the thermal conductivity was the most influential property, whereas Young's modulus was the most influential for structural modeling. Finally, the effect of different process parameters on the results were explored, and the authors

found that the raster speed of the laser was the most influential process parameter. Mukherjee et al. [14] developed a three-dimensional model of additive manufacturing, which was then experimentally validated. The model consisted of ten straight layers. The model was then used to determine the effect of process parameters on the structural behavior of the manufactured part. The authors state that a reduction in layer thickness can reduce residual stresses. However, the latter comes at the cost of increased warpage, and so this trade-off must be fully understood and balanced for each application. It is worth noting that simple geometries were used in most of the above cited studies such as straight slabs [8–12].

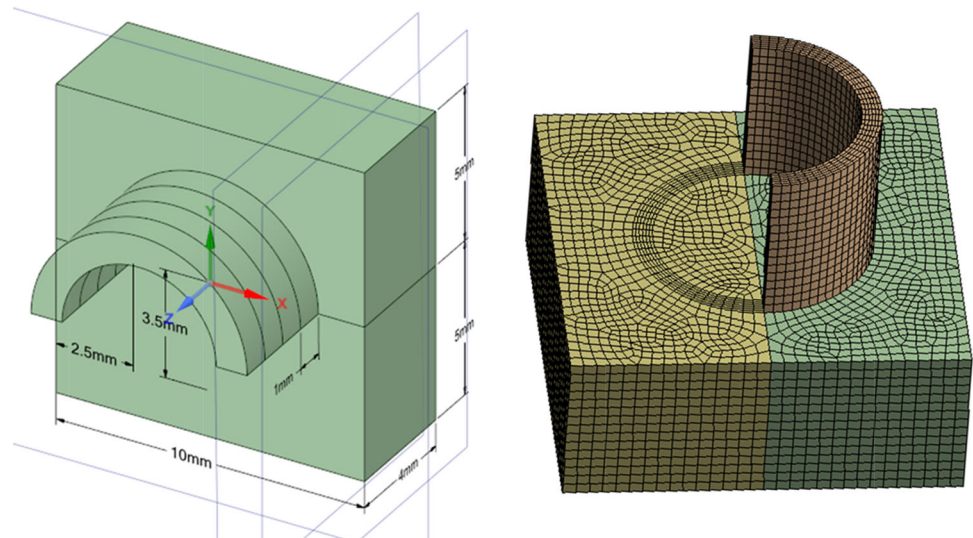
A trial-and-error approach is currently used in the industry to minimize the residual stresses and distortion in AM [15, 16]. However, this approach is time-consuming and costly. Therefore, numerical modeling of AM provides an alternative approach to predict the thermal and mechanical behavior of the AM process and to optimize its controlling parameters (e.g., power of the laser beam, scanning speed, and direction) [17–19]. The accuracy of the numerical results depends on the use of accurate transient temperature variations which consequently influence both the residual stresses and strain.

Many of the cited studies in AM used simplified models such as a stack of straight layers and that further analysis is needed to fully understand the thermo-mechanical behavior of the AM process in different shapes of manufactured parts. In the present work, we extend the work outlined in [7] to conduct a detailed analysis of thermo-mechanical behavior of the additive manufacturing process. Specifically, we seek to analyze the impact of the temporal variation of the temperature field (thermal history) due to the rastering direction of the laser beam on temperature, strain, stress and deformation. To the best knowledge of the authors, a detailed investigation into the effect of the thermal history resulting for changing the direction of rastering (scanning) of the laser beam on thermal stresses and deformation has not been studied in realistic, albeit simplified, machine components. This investigation will be structured into the following sections: Methodology, Results and Discussion, Thermo-Structural, and Conclusions.

2 Methodology

Khanafer et al. [7] has a detailed description of the problem geometry, mathematical model and solution methodology along with validation studies, hence only a brief description of these aspects is provided for the benefit of the reader. The schematic of the problem under consideration is illustrated in Fig. 1. For the mesh generation, solid 8-node hexahedron elements were used. The elements have temperature and displacement degrees of freedom depending on the corresponding thermal and structural analysis. The entire mesh

Fig. 1 Geometry and mesh of the model used in the present investigation



consisted of a total number of 36,106 elements and 8327 nodes. The machine component was assumed to be a half-cylinder with a 3-mm radius and was built by superimposing four single layers with a thickness of 1 mm each, which was selected as a compromise to minimize CPU time, consequently this need to be taken into consideration when reading simulation results and consider them as trends. The half-cylinder is built on a base with dimensions of 10 mm × 10 mm × 4 mm as shown in Fig. 1. The moving laser source was modeled using Gaussian distribution function as described in [7] As follows:

$$S = C_2 * \exp \frac{-\{(x)^2 + (y - v * t)^2\}}{C_1^2} \quad (1)$$

where S is the heat flux on the surface, C_1 is the laser beam radius (1 mm in this study), C_2 is the source power intensity ($= 4.15 \times 10^7 \text{ W/m}^2$), (x, y) are the instantaneous position of the heat flux center, v is the heat source velocity, and t is the time. In this study, the substrate and the powder layers were initially kept at a constant temperature as follows:

$$T(x, y, z, t = 0) = T_o \quad (2)$$

Also, a constant boundary temperature was used for the bottom surface of the base substrate as follows:

$$T(x, y, z = 0) = T_o \quad \text{for } t > 0 \quad (3)$$

A heat loss boundary condition was used for all other surfaces. This boundary condition takes into an account the heat losses due to both convection and radiation and is expressed as:

$$k(T)(\nabla T \cdot \vec{n}) = h(T_s - T_\infty) + \sigma \varepsilon (T_s^4 - T_o^4) - S \quad (4)$$

where k is the temperature dependent thermal conductivity, h is the convection heat transfer coefficient, T_s is the surface temperature updated at each time step, T_∞ is the ambient temperature, T_o is the temperature of the walls surrounding the substrate which is assumed equal to the ambient temperature in this work. The material utilized in this investigation was Ti–6Al–4V alloy due to its high strength—to—weight ratio at high temperature. All the properties (e.g., thermal conductivity, density, and specific heat) input into ANSYS software were assumed dependent on temperature only since high range of temperature were anticipated in this study [7]. The finite element commercial software (ANSYS) was used to compute the temperature, stress, strain and deformation in a coupled self-consistent manner. The physical dimensions for the problem under consideration were chosen to strike a balance between computational time and developing a qualitative understanding of the role process parameters in thermal stresses during additive manufacturing. Gan et al. [19] reported that building six-layers each 0.15 mm required 36 h using $12 \times 2.5 \text{ GHz}$ CPU and 24 GB memory.

3 Results and discussion

The additive manufacturing process was analyzed numerically in this study to show the effect of varying the laser scan strategy on the thermal and mechanical behavior of the process. Using the developed computational model, the effect of varying the laser direction was investigated using two cases. In case 1, the laser beam moves in a counterclockwise (CCW) direction during the deposition of all layers while in case 2, the odd-numbered layers were deposited in a CCW direction, and for the even-numbered layers the laser beam moved in the opposite direction (clockwise/CW). Both cases

are described by the corresponding angular velocity, $\vec{\omega}_1$ and $\vec{\omega}_2$ given below.

Case 1, CCW:

$$\vec{\omega}_1 = \frac{v}{R} \vec{e}_z \tag{5}$$

Case 2, alternating:

$$\vec{\omega}_2 = \begin{cases} \frac{v}{R} \vec{e}_z \text{ Layers : 1, 3} \\ -\frac{v}{R} \vec{e}_z \text{ Layers : 2, 4} \end{cases} \tag{6}$$

Figure 2 shows the temperature distribution in the first layer as the laser beam traverses in the CCW direction from $\theta = 90^\circ$ to $\theta = -90^\circ$. As expected, the location of the peak temperature occurs at the location the laser beam is focused. Hence, after the deposition of the first layer with the laser beam traversing in the CCW direction, the peak temperature of 1976 K is seen at $\theta = -90^\circ$.

Figure 3 shows a comparison of the temperature distribution in the component as the layers are successively deposited in the CCW and alternating mode. For the CCW case, the laser beam is brought back to the $\theta = 90^\circ$ position to begin the deposition of the second layer, whereas for the alternating case, the laser beam begins depositing from $\theta = -90^\circ$. Since the location of heat addition moves to the $\theta = 90^\circ$ position for the beginning of the second layer in the CCW case, the material near $\theta = -90^\circ$ position can lose heat by transferring it to the base and to cooler regions on the deposited layer ($\theta < -90^\circ$) while the second layer is being deposited. This does not occur in the alternating mode where the laser beam traverses back from the heated regions near $\theta = -90^\circ$. This leads to an overall higher peak temperature after the deposition of the second layer in the alternating case as compared to the CCW case. After the deposition of the second layer, the relative temperature difference between the two cases was about 0.6% and the corresponding temperatures for Cases 1 and 2 were 2169 and 2182 °C, respectively. For each successive layer the alternating mode shows a higher peak temperature as compared to the CCW mode due to the reason discussed above. The values of the relative temperature difference between the two cases increases to around 3% after the third and fourth layers were deposited. It is also seen that the peak temperature in the component increases as the cooling effect of the substrate diminishes as the layers move further away from the base.

Figure 4 shows the distribution of the magnitude of the temperature gradient in the part for both cases at the time instant after the deposition process was completed. In Case 1 (CCW), the maximum magnitude of the temperature gradient was 688.8 °C/mm while a higher value of 763 °C/mm was reached in Case 2 (alternating). In both cases, the maximum value occurred in the first layer under the end point of

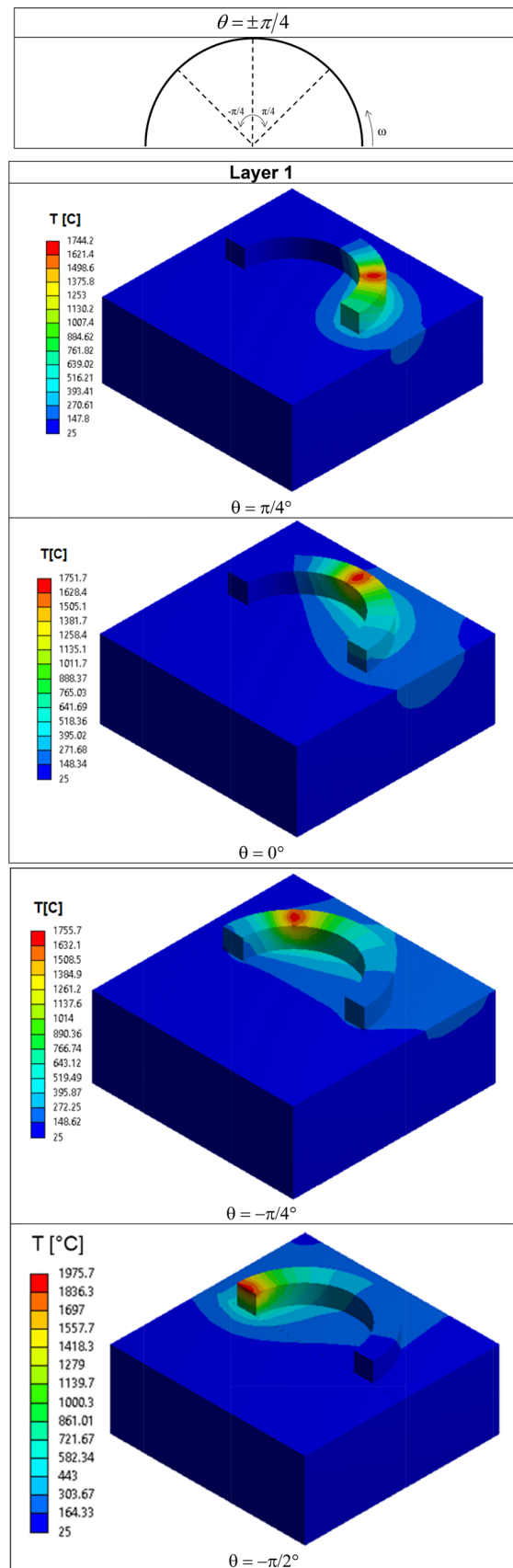


Fig. 2 Temperature distribution as the laser beam traverses from $\theta = \pi/2^\circ$ to $\theta = -\pi/2^\circ$ (CCW)

Fig. 3 Effect of varying the direction of the laser beam speed on the temperature distribution with each additional layer

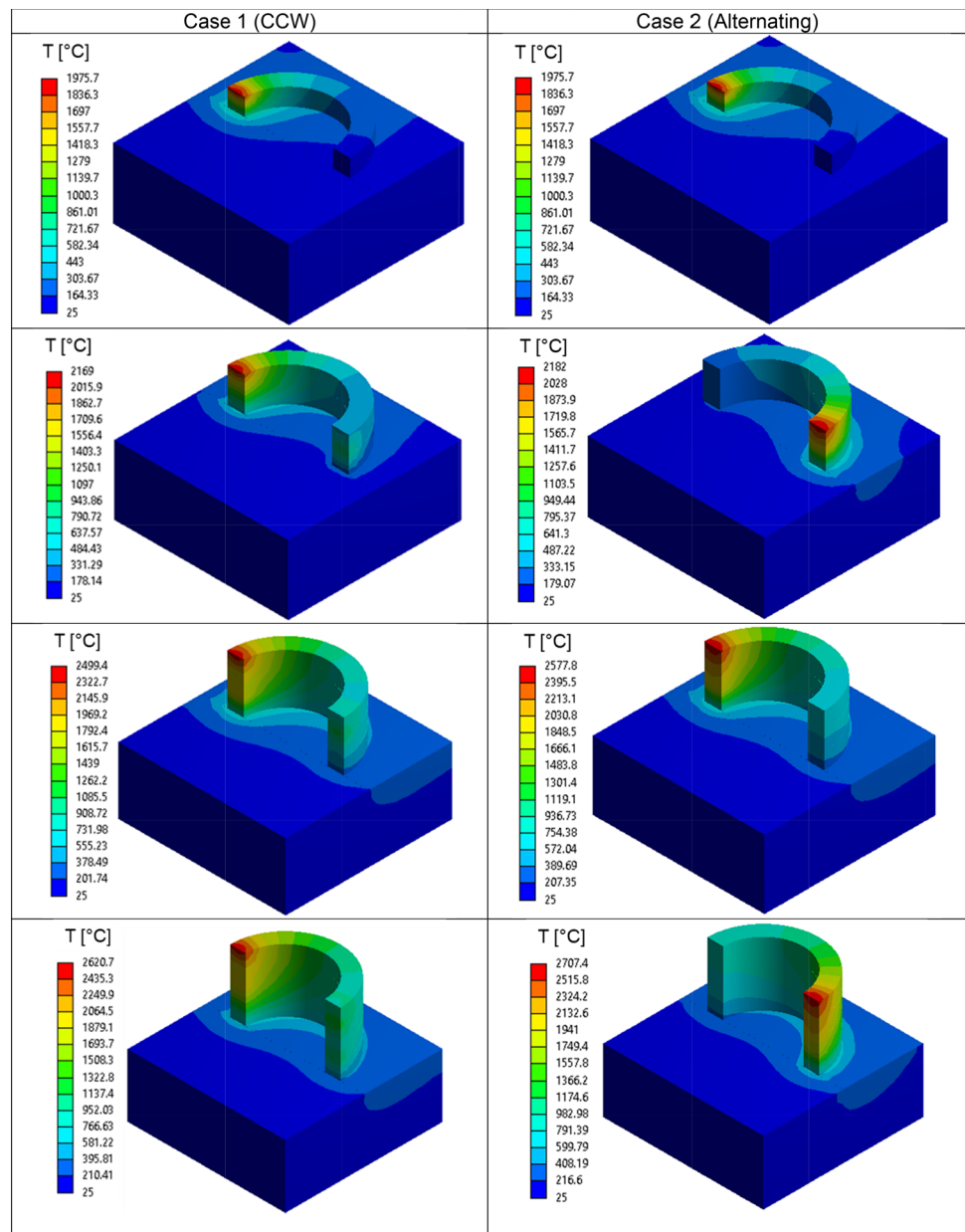


Fig. 4 Effect of varying the direction of the laser beam speed on the temperature gradient

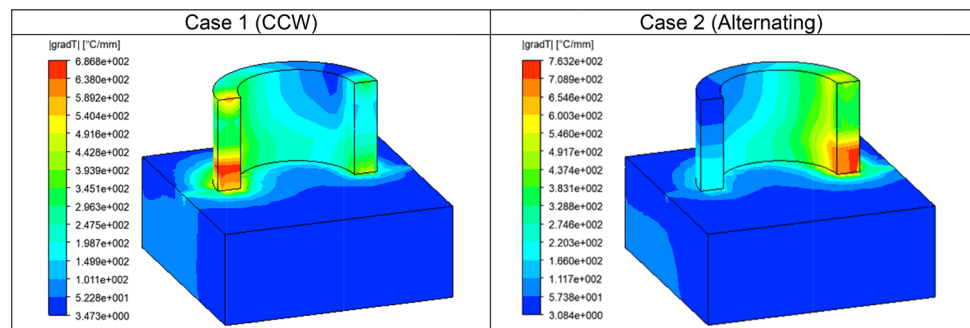
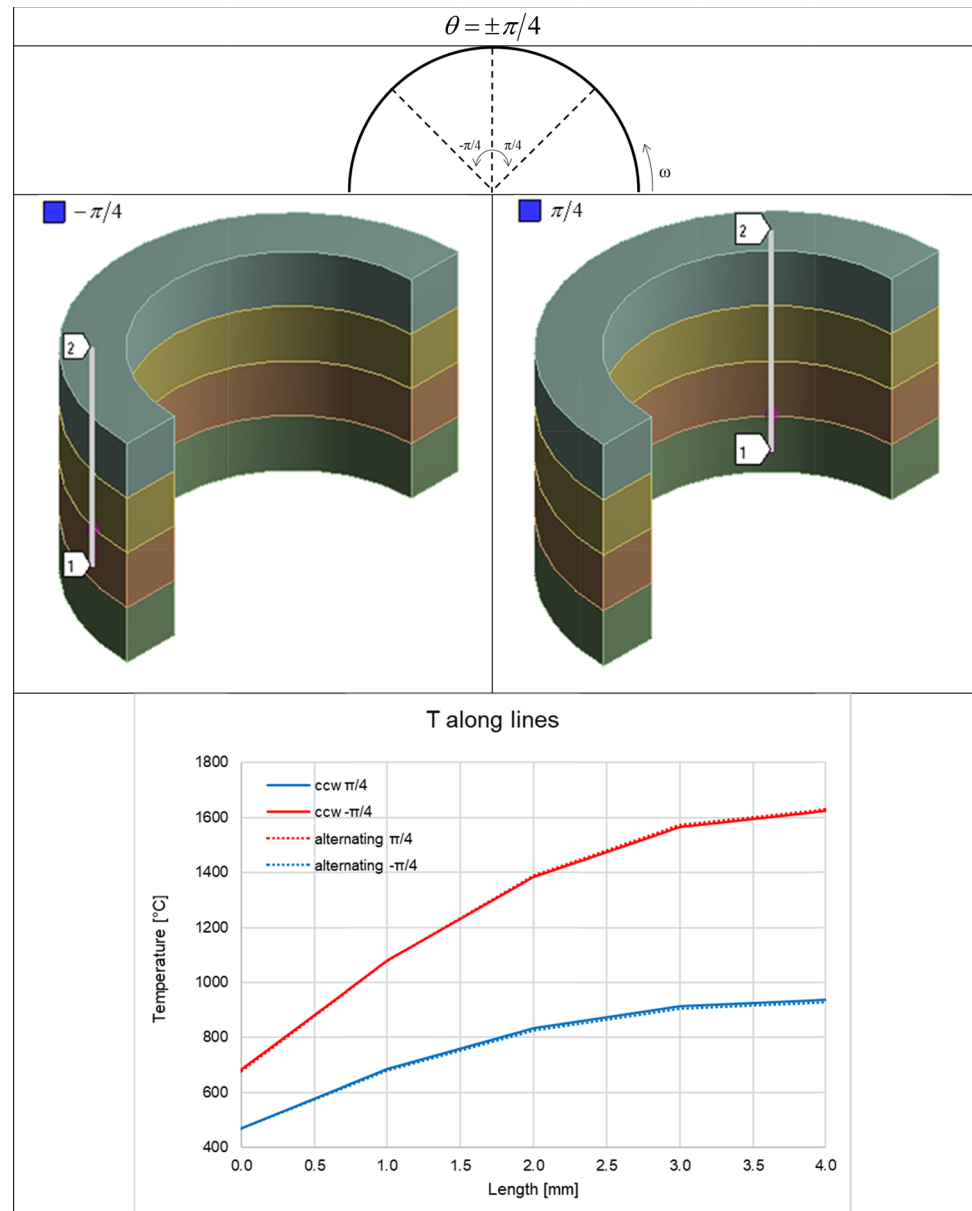


Fig. 5 Effect of varying the direction of the laser beam speed on the temperature profiles along a vertical plane passing through different layers



deposition in the last layer. This behavior can be explained on the basis of the deposition pattern. If the time for the laser beam to traverse its path from one end to the other is τ seconds, then for the CCW case, any particular location in the component has the heat source directly above it after a time duration of τ seconds. However, for the alternating case, the time duration when the laser beam is directly above a given angular can vary between 0 and 2τ seconds. Hence the relative time for cooling by heat conduction is widely varying in the alternating case as compared to the CCW case, thus leading to a larger thermal gradient.

Figure 5 compares the temperature profiles along two vertical lines at symmetrical positions with respect to the center line of the body (lines 1–2 at $\theta = 45^\circ$ and line 3–4 ($\theta = -$

45°). The temperature values correspond to the time instant after depositing the last layer. As expected, the temperature variation along the height of the component for each of these locations is almost identical for both the CCW and alternating cases (on account of their symmetrical location). Furthermore, the temperature gradient along the vertical direction decreases near the top surface. The higher magnitude of the temperature gradient near the substrate was also observed in Fig. 4.

The effect of changing the direction of the laser beam speed on the temporal variations in temperature at different heights (at $\pi/4$) is depicted in Fig. 6. The thermal cycles at the shown positions are studied during the deposition process and a comparison between the corresponding situations

Fig. 6 Effect of changing the direction of the laser beam speed on the temporal variations of temperatures at different heights (at $\pi/4$)

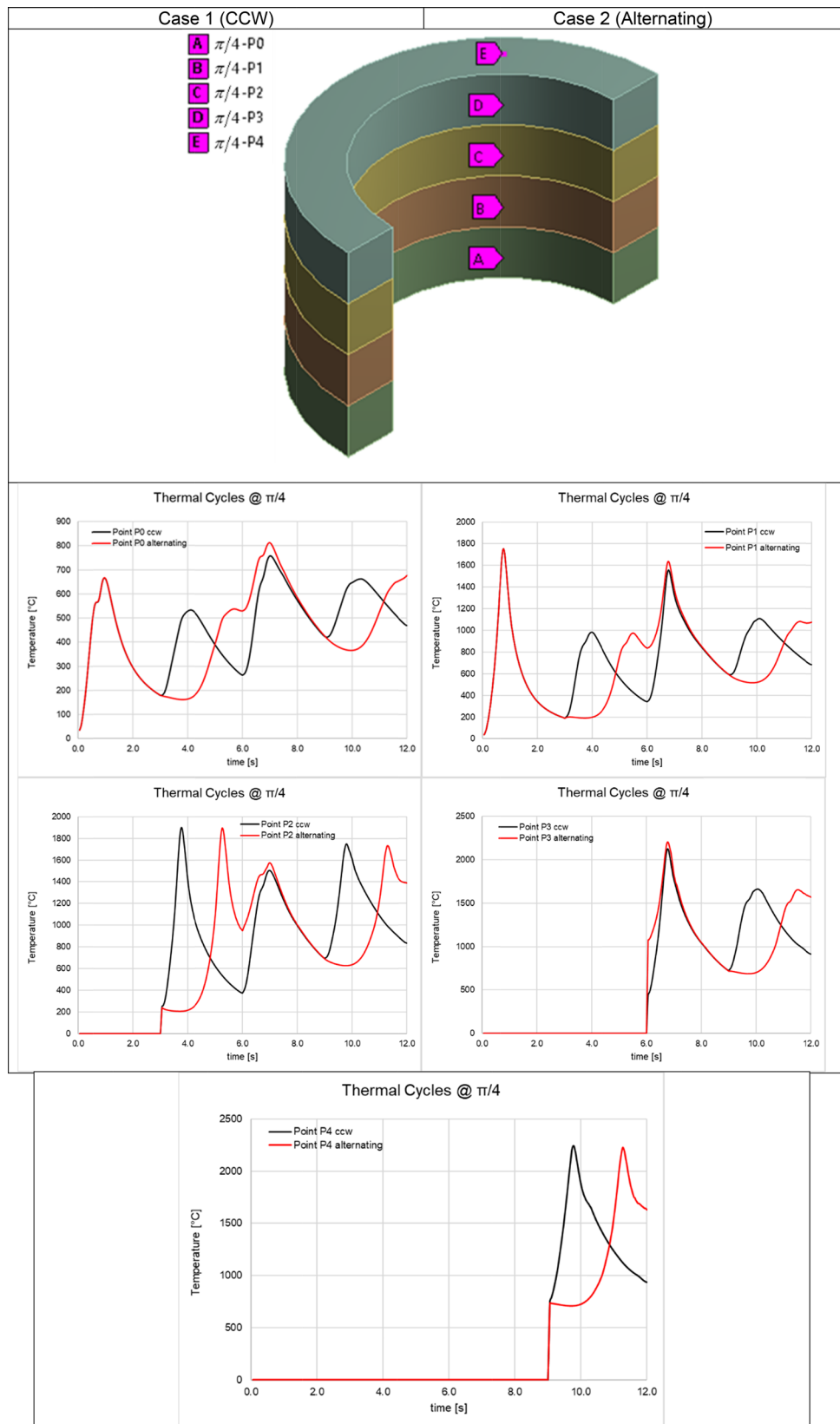
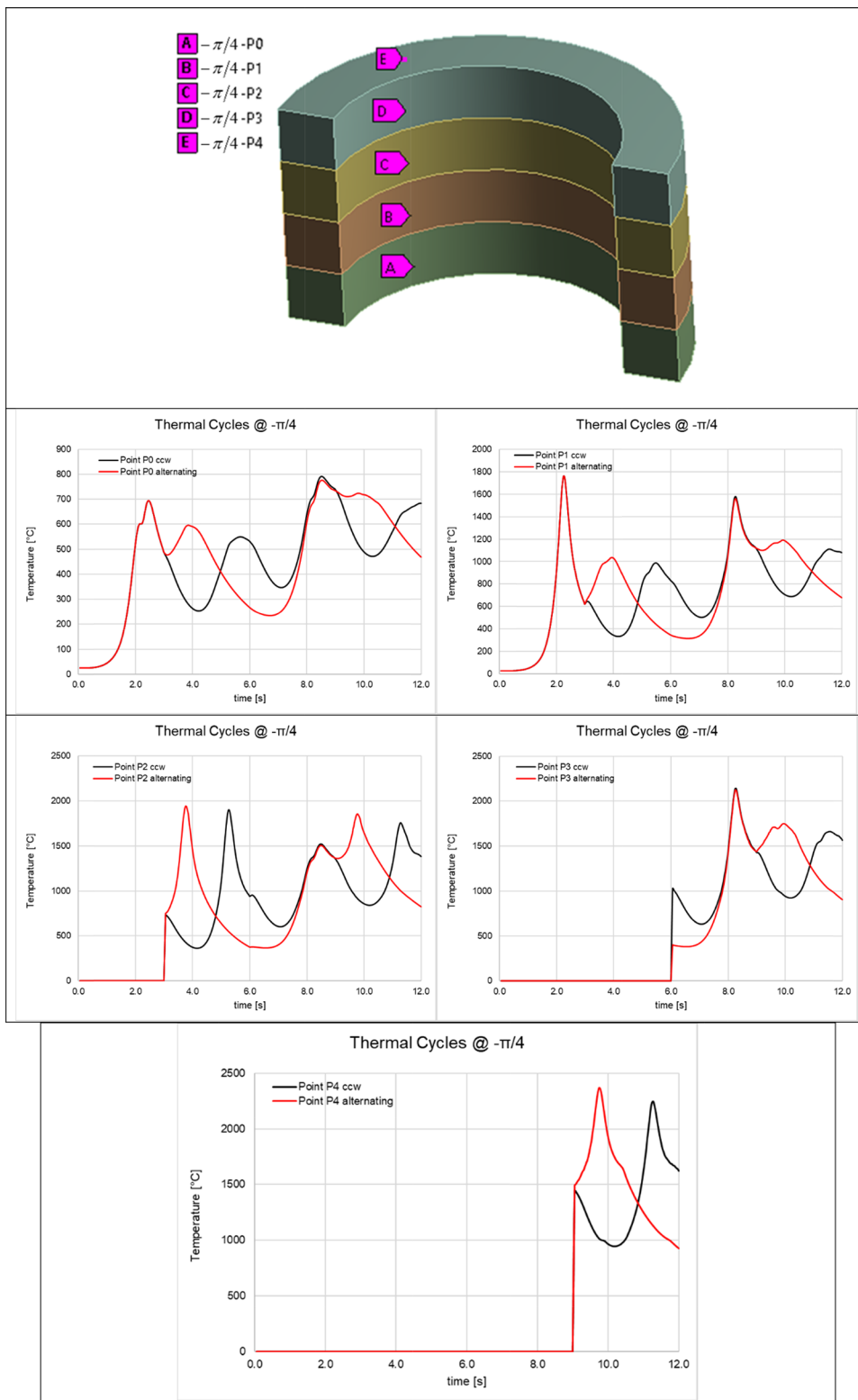


Fig. 7 Effect of changing the direction of the laser beam speed on the temporal variations of temperatures at different heights (at $-\pi/4$)



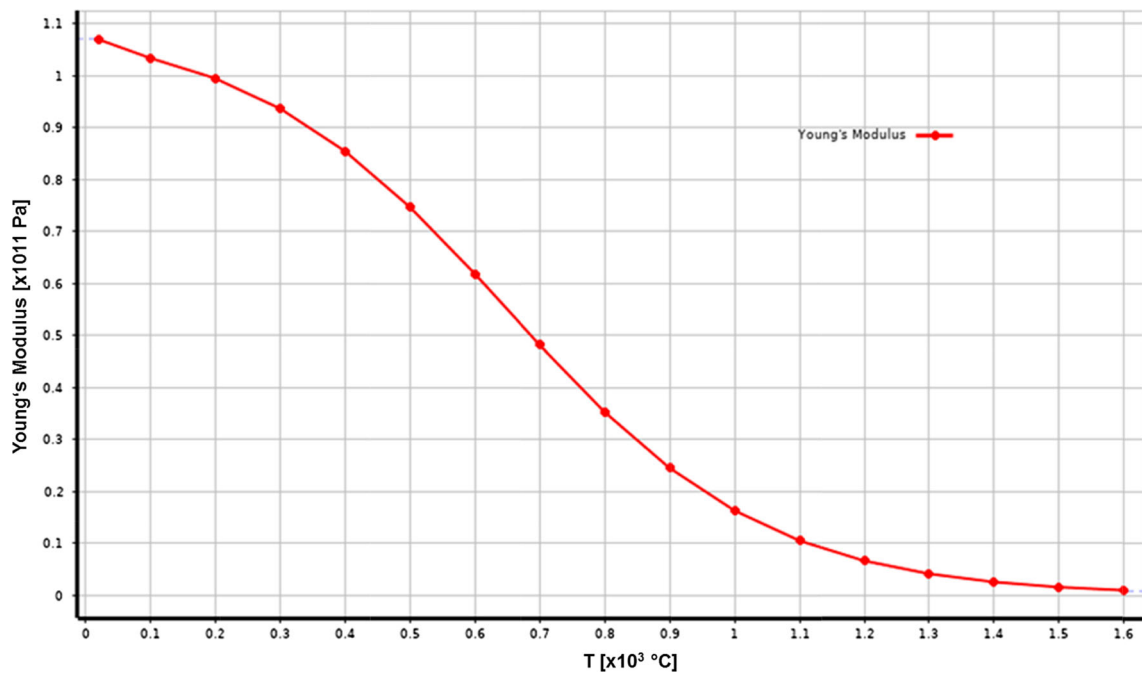
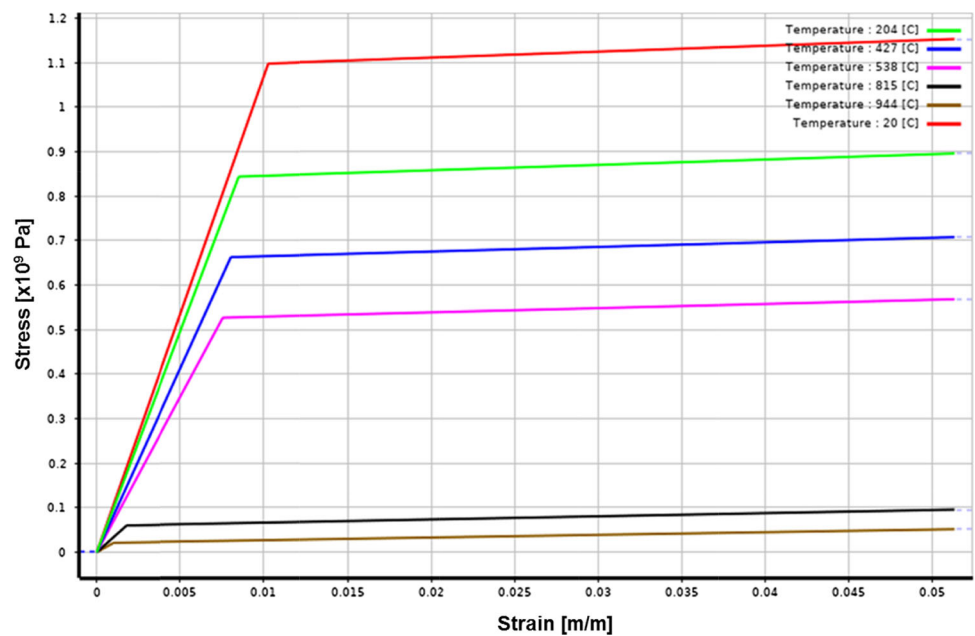


Fig. 8 Young's modulus as a function of temperature

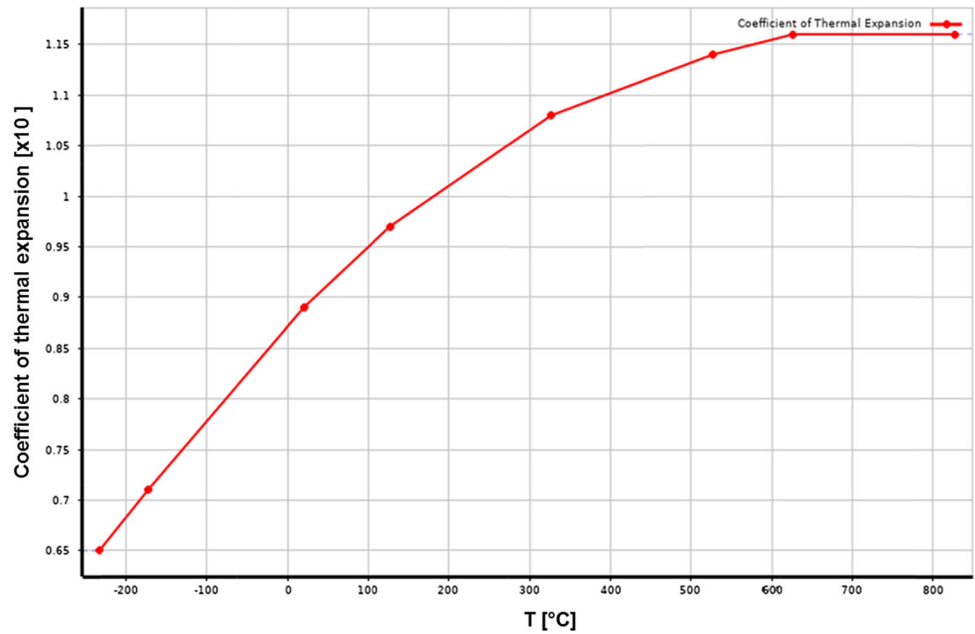
Fig. 9 bilinear isotropic hardening curves for different temperatures



in Cases 1 and 2 is presented. The considered points lay on the surfaces of the substrate and the deposited layers. At positions A and B (Points P0 and P1), the time history curves show a similar behavior except that higher temperature values are reached at position B on the top surface of layer 1, since this point receives the heat directly from the laser source while heat is conducted to the point on the surface of the substrate. The curves are characterized by four peaks, corresponding to the time instants at which the laser head passes through

the points of the four layers. However, a small lag exists owing to the time needed to conduct the absorbed heat in the colder downward direction. For both depositing directions (Cases 1 and 2), the curves are identical until the first layer is deposited. Furthermore, in Case 1 the curve peaks are separated by almost the same period of time. In Case 2, the time period between the first and the second peaks is greater than between the second and the third peaks. This is due to the fact that the laser head travels different path lengths in the

Fig. 10 coefficient of thermal expansion as a function of temperature



analyzed cases until the corresponding position is reached. Moreover, it can be seen that the temperature values reached at the peak locations do not depend on the direction of deposition. It is also evident that in Case 2, a larger time period for cooling exists between layers 1 and 2 as well as 3 and 4. The curves showing the temperature time history at the positions in the added layers have similar characteristics, except that after each track the temperature peaks reach higher values owing to the preheated body. The effect of changing the direction of the laser beam speed on the temporal variations in temperature at different heights (at $-\pi/4$) is shown in Fig. 7. The time history curves are displayed for the corresponding points at symmetrical positions with respect to the vertical axis. For this angular location and for Case 1, the maximum temperature values are also separated by similar time periods. In contrast, for Case 2 the temperature peaks corresponding to layers 1 and 2 as well as 3 and 4, are separated by smaller time intervals than for layers 2 and 3. Also at these positions the maximum temperatures increase after each deposited layer.

3.1 Thermo-structural results

The thermo-structural investigation is carried out by decoupling the analysis into a transient heat transfer process followed by a structural analysis. The temperature field from each time increment provides the thermal load for the mechanical analysis. The material behavior is assumed to be elasto-plastic with isotropic strain hardening. The parameters of the applied constitutive law are temperature dependent. These include the Young’s modulus, the yield stress, the strain hardening modulus and the coefficient of thermal

expansion. The material behavior characteristics are displayed in the Figs. 8, 9 and 10 [7].

As described in the thermal analysis, the deposition process is modeled using the element “birth and death” procedure available in the ANSYS software. In Fig. 11, the resulting distribution of the thermal strain is displayed after the deposition of each layer for both tracking directions. The thermal deformations are described in this study by the thermal strain tensor ϵ_{ij}^{th} given by:

$$\epsilon_{ij}^{th} = \alpha * \Delta T * \delta_{ij} \quad i, j = 1, 2, 3 \tag{7}$$

with

$$\Delta T = T - T_{ref} \tag{8}$$

and

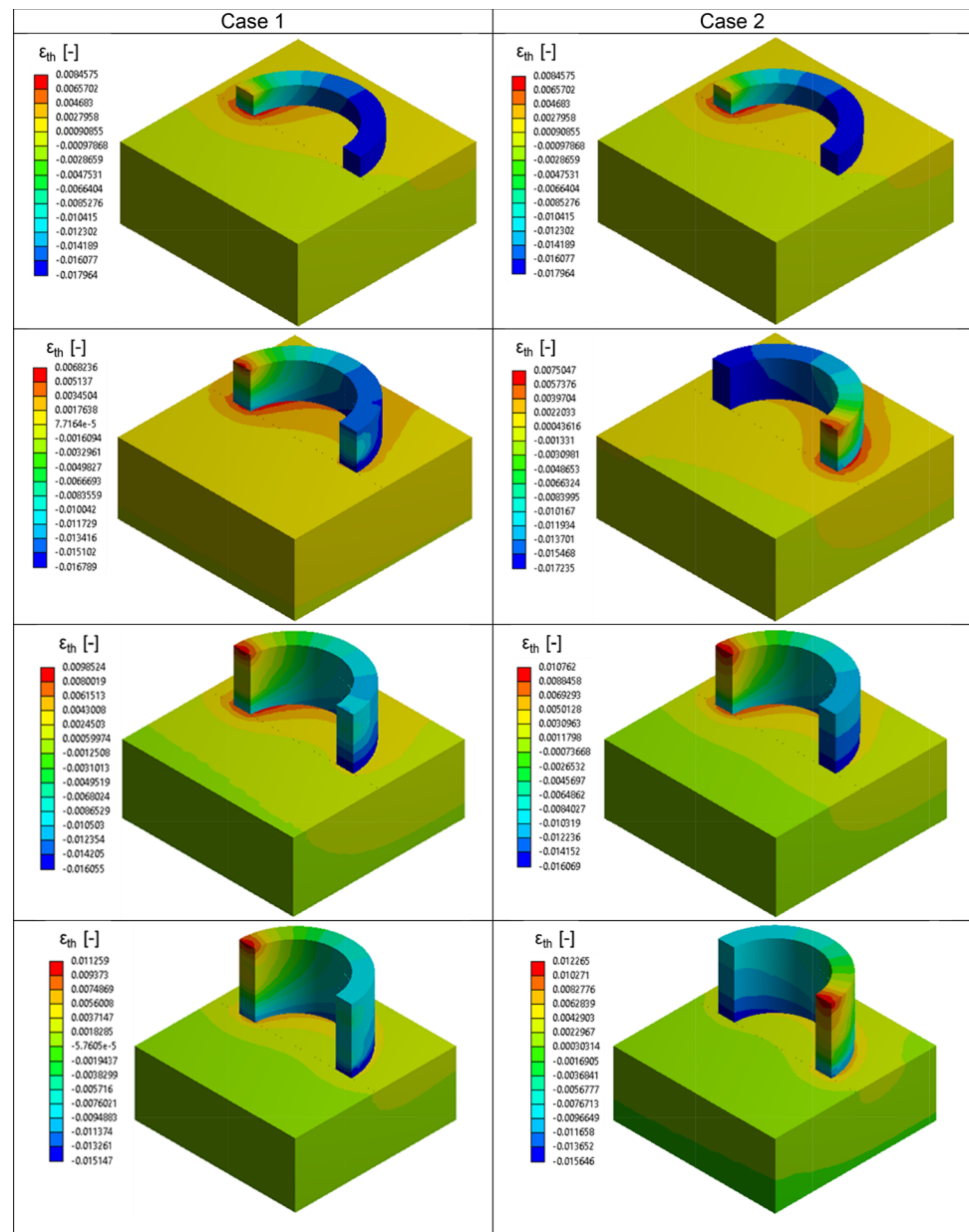
$$\alpha = \frac{1}{T - T_{ref}} * \int_{T_{ref}}^T \alpha'(\vartheta) * d\vartheta \tag{9}$$

The Kronecker-Symbol δ_{ij} represents a unit tensor such that:

$$\delta_{ij} = \begin{cases} 1, & i = j \\ 0, & i \neq j \end{cases} \tag{10}$$

α' is the thermal expansion tangential coefficient, while T and T_{ref} are the local and reference temperatures in the stress-free state, respectively. The reference temperature must be defined in this investigation in order to evaluate the thermal strains. In this analysis for the substrate plate, the room

Fig. 11 Distribution of thermal strain (ϵ_{th}) at the end of deposition of each layer

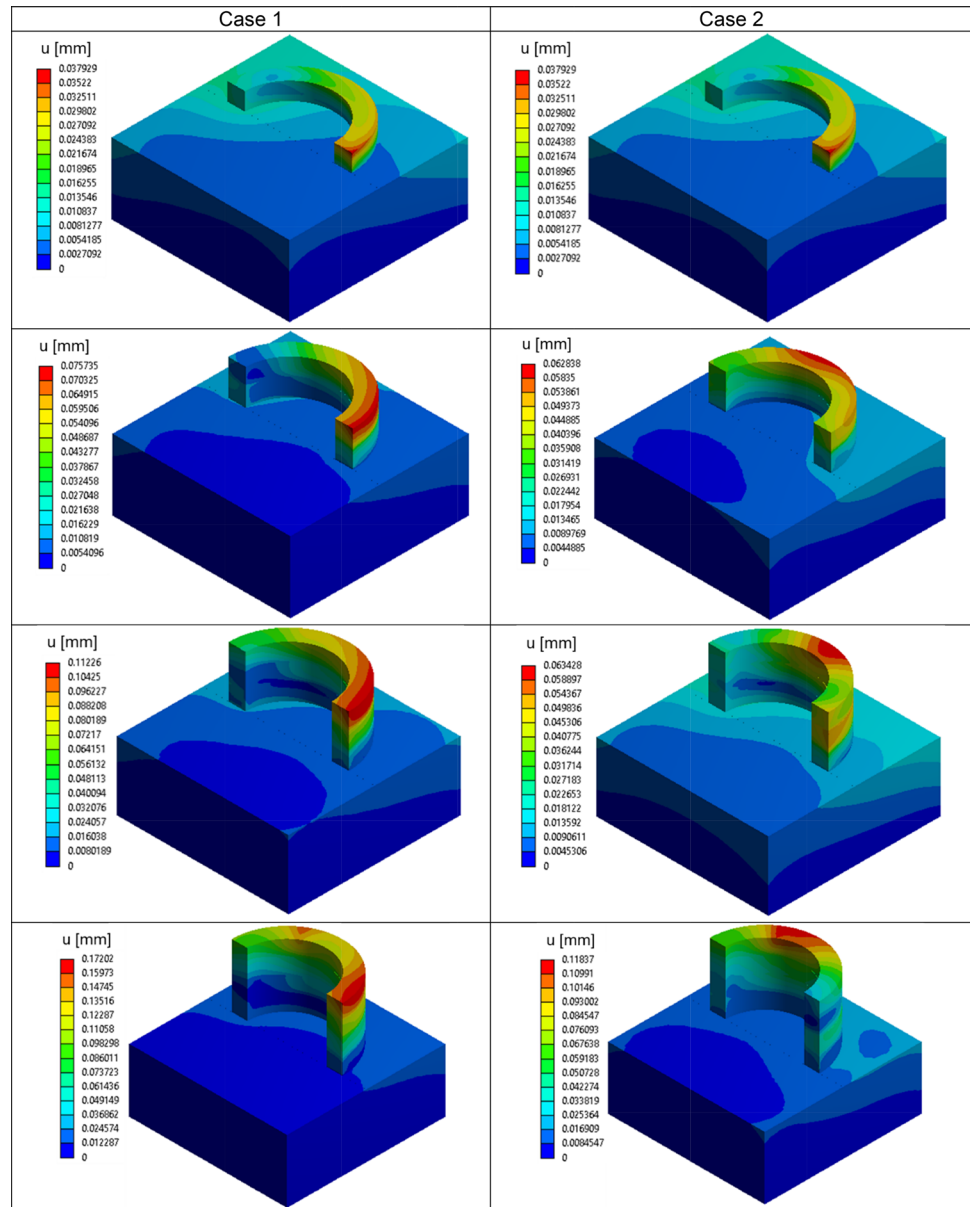


temperature is considered as the stress-free state. For the Ti–6Al–4V layers, the liquidus temperature (1655 °C) at which the thermal strains begin to accumulate is defined as the reference temperature. After the first layer is deposited, the maximum absolute values of thermal strain occur in the starting region of deposition and are about 1.8%. Due to successive heating, the temperature of the deposited layers increases. Consequently, the difference between the local and the reference temperature reaches smaller absolute values, which leads to less thermal strains. This trend applies to both tracking directions. Furthermore, the resulting thermal strains in Case 2 are slightly higher than those in Case 1, as

can be seen in Fig. 11. The results indicated that the maximum thermal strain of Case 2 (alternating) is higher than in Case 1 by 9–10% in all deposited layers. It is also evident from the figure that the locations of the maximum absolute values of the thermal strains depend on the depositing direction. In Case 1, these values are always observed under the starting point of the laser head in the interface plane between the first layer and the substrate body. In Case 1, this is the same position for all layers; on the other hand, in Case 2 the position changes according to the initial point from which the layer is deposited.

Figure 12 shows the deformation field in the body after tracking each layer. When the first layer is completed, the

Fig. 12 Deformation distribution (u) at the end of deposition of each layer

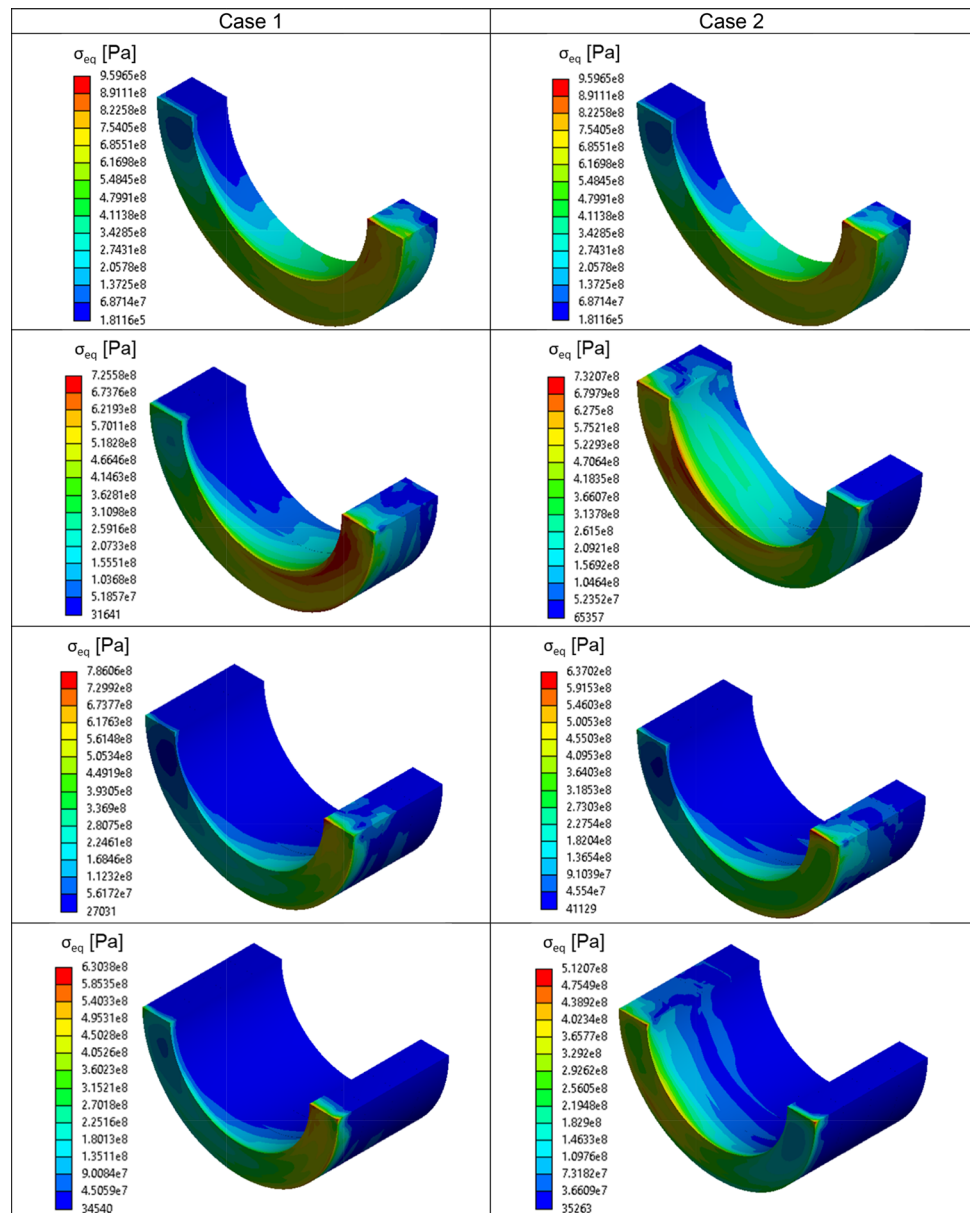


right region is subjected to the maximum magnitude of thermal strain, as observed in Fig. 11. Since the upper right corner can freely deform, this zone experiences the maximum deformation. In both cases the deformation rises after the successive deposition of further layers. However, in Case 1 the maximum deformations reach higher values than in Case 2. This could be due to the greater thermal gradient in Case 2, as was observed in Fig. 4. The results of the deformation shows that Case 1 has higher deformation than in Case 2 by 20% in layer 1, 75% in layer 3, and 45% in layer 4, respectively. The deformation of regions having higher values is prevented because of the non-uniform temperature field regions with smaller values of the term $|T - T_{ref}|$ in Eq. (8). Owing to this fact, the maximum deformations in Case 2 appear in the

middle of the deposited layers and not at the corner as in Case 1.

The equivalent (von Mises) stress distribution in the deposited layers is presented in Fig. 13. High stresses appear in the interface region of the substrate, and they take their maximum value (959.6 MPa) after depositing the first layer. Since the deposited layers are attached to a colder body with a higher structural stiffness, this would prevent the deformation of the tracked layers in the contact region. Owing to this fact, higher stress values are predicted in this area in comparison to the upper layers that have more freedom to deform. Furthermore, carrying out the deposition process according to Case 2 would in general induce 120–150 MPa less in concentrated stresses than in Case 1. Moreover, the locations of

Fig. 13 Von Mises stress (σ_{eq}) at the end of deposition of each layer



the maximum stress values correspond very well with the positions of maximum thermal strain magnitudes, observed in Fig. 11. Accordingly, in Case 1 the maximum stresses appear in the same area for all layers, while in Case 2, adding a new layer leads to a change in these positions.

In Figs. 14, 15, 16 and 17, the maximum shear stress distributions are displayed in planes at different elevations, and the resulting stresses are compared after each additional layer. Figure 14 displays the distribution of the maximum shear stresses in the interface plane between the substrate body and the first layer. The shear stress concentration positions depend on the direction of deposition, and they follow the same trend observed in the thermal strain and von Mises

stress analysis. Furthermore, carrying out the deposition process according to Case 1 leads to higher shear stresses of 60–110 MPa. These are responsible for crack initiation in the corresponding region. Figure 14 also shows an interesting result that the maximum shear stress in the interface plane between the substrate and the first layer decreases with depositing more layers for both Cases. However, Case 1 still exhibits the larger shear stresses.

The upper surface of the first layer experiences less shear stresses than the bottom surface, as can be seen in Fig. 15. After the first layer has been deposited, the maximum value that appears on plane 0 is over 480 MPa, while a stress value of 252 MPa is reached on plane 1. This is due to the fact that points on plane 1 have more freedom to deform than

Fig. 14 Maximum shear stress: τ_{\max} on the substrate at the end of deposition of each layer

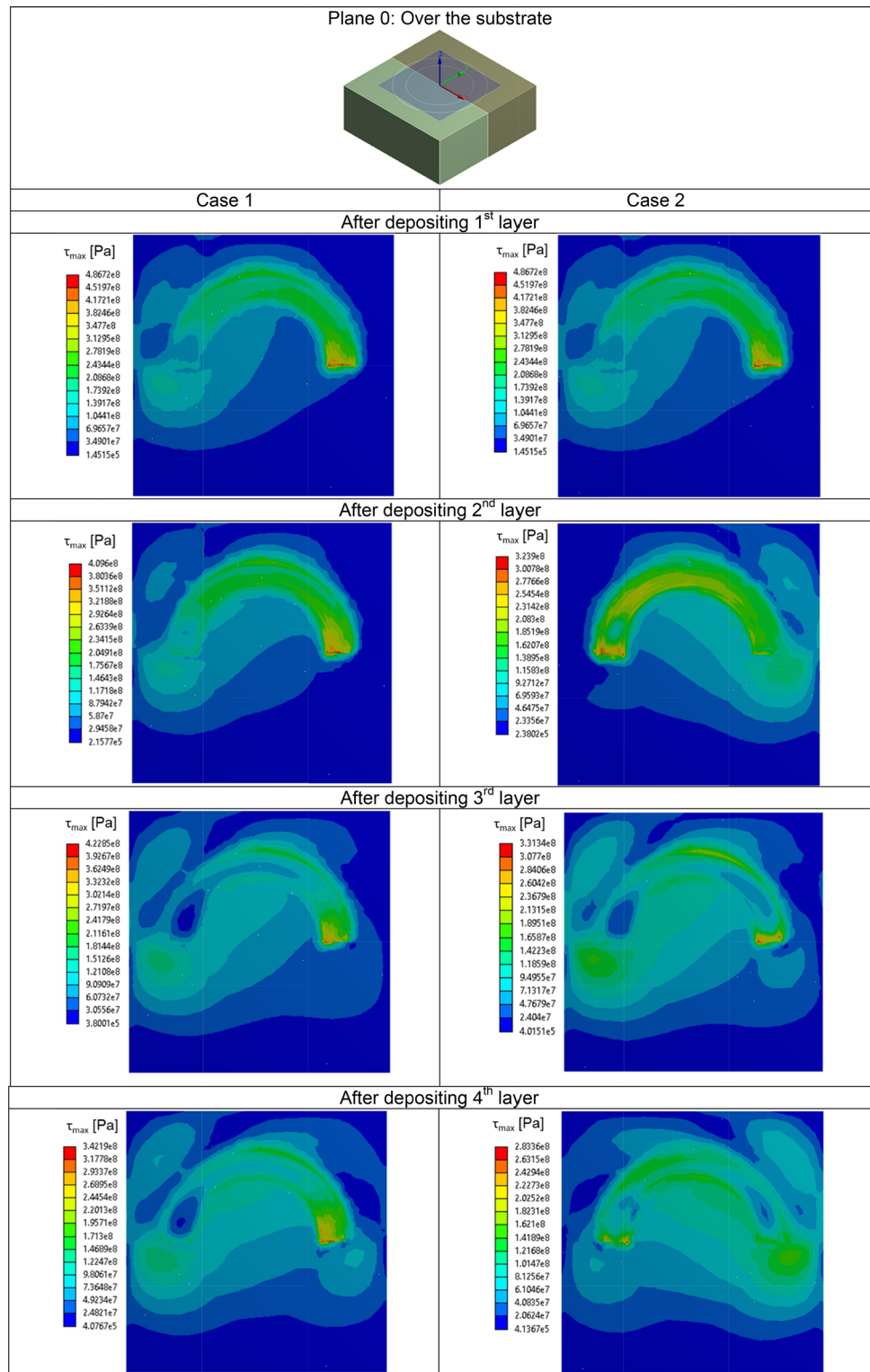


Fig. 15 Maximum shear stress: τ_{\max} over layer 1 at the end of deposition of each layer

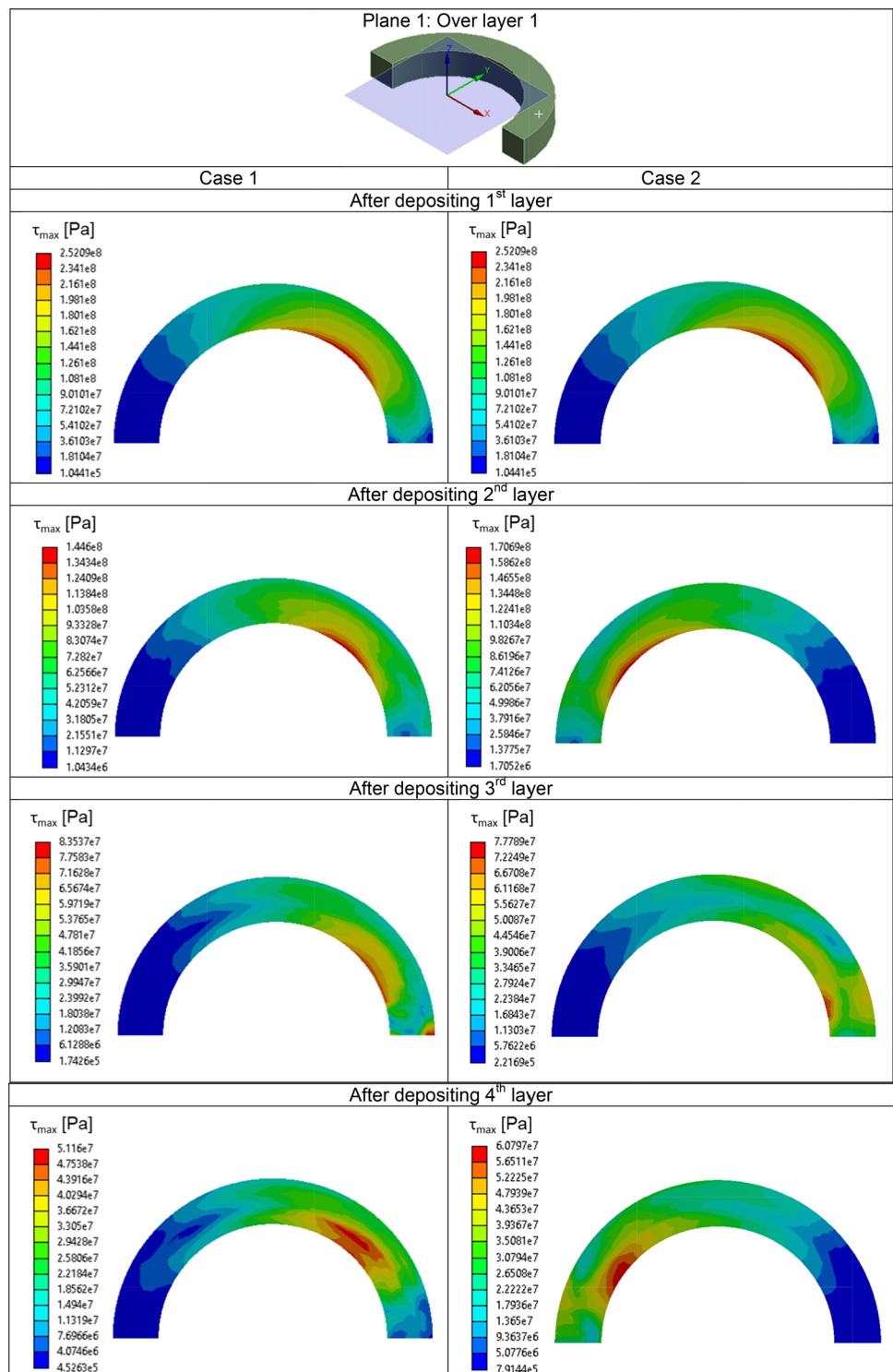
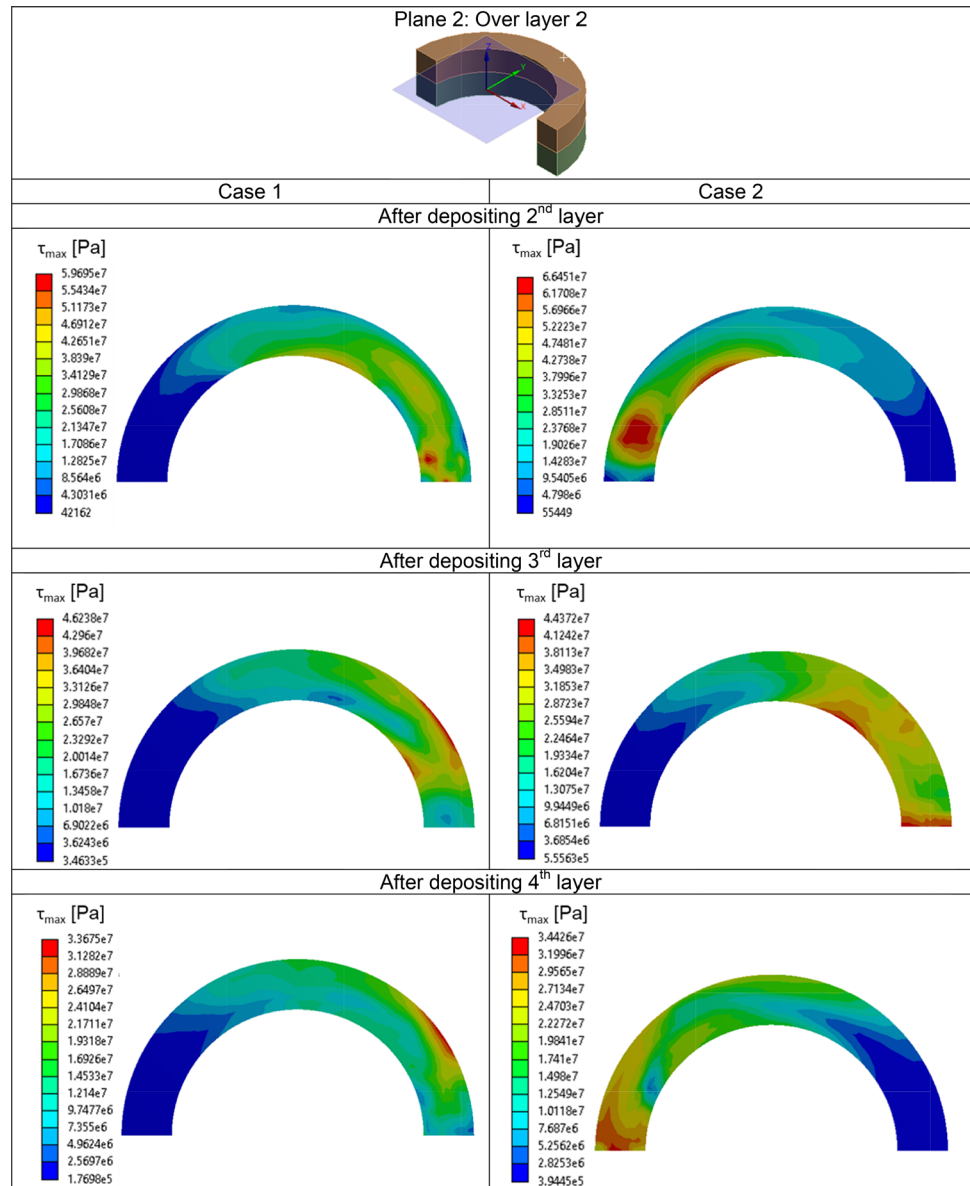


Fig. 16 Maximum shear stress: τ_{\max} over layer 2 at the end of deposition of each layer



points on plane 0; these points are constraint by the substrate body with the higher structural stiffness. With each additional layer, the shear stresses in plane 1 decrease. After the last layer has been deposited, the maximum values of 50 MPa in Case 1 and 60 MPa in Case 2 have been reached. Owing to the absorbed heat, the temperature of the structure increases with each deposited layer as was observed in Fig. 5. The high temperatures lead to lower material stiffness and consequently, to reduced stresses. The same trend is observed in the planes presented in Figs. 16 and 17. In Fig. 18, the time history of the stress is presented for points A and B at the corners of the first deposited layer. Since the elements of the entire layer are activated at the time instant when the laser head starts to move, point A must be at a lower temperature than point B, where the heat input starts. Keeping in mind the fact that the

melting temperature is used as the reference point for evaluating the thermal strains, point A experiences an increased thermal strain that leads to a higher stress than that at point B. Until the first layer has been deposited (at the time instant three seconds), the curves for point A are identical in Case 1 as well as Case 2. Time instants of local minimum stresses correspond to times at which the laser head reaches the closest positions to the considered points. In Case 1 this happens four times, corresponding to the time instants 0 s, 3 s, 6 s and 9 s at point A, and at point B these time instants are after 0 s, 3 s, 6 s and 9 s. In Case 2, two local minima and consequently, fewer stress peaks, exist in the curve owing to the oscillating motion of the laser head.

Fig. 17 Maximum shear stress: τ_{max} over layer 3 at the end of deposition of each layer

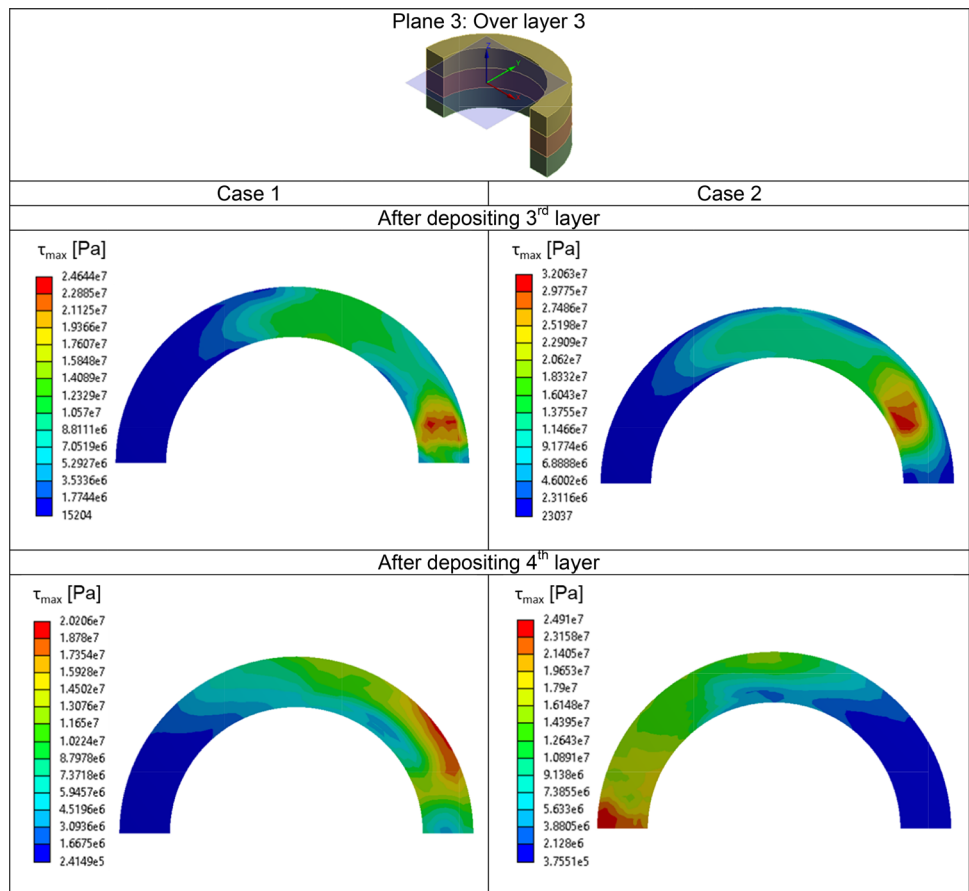
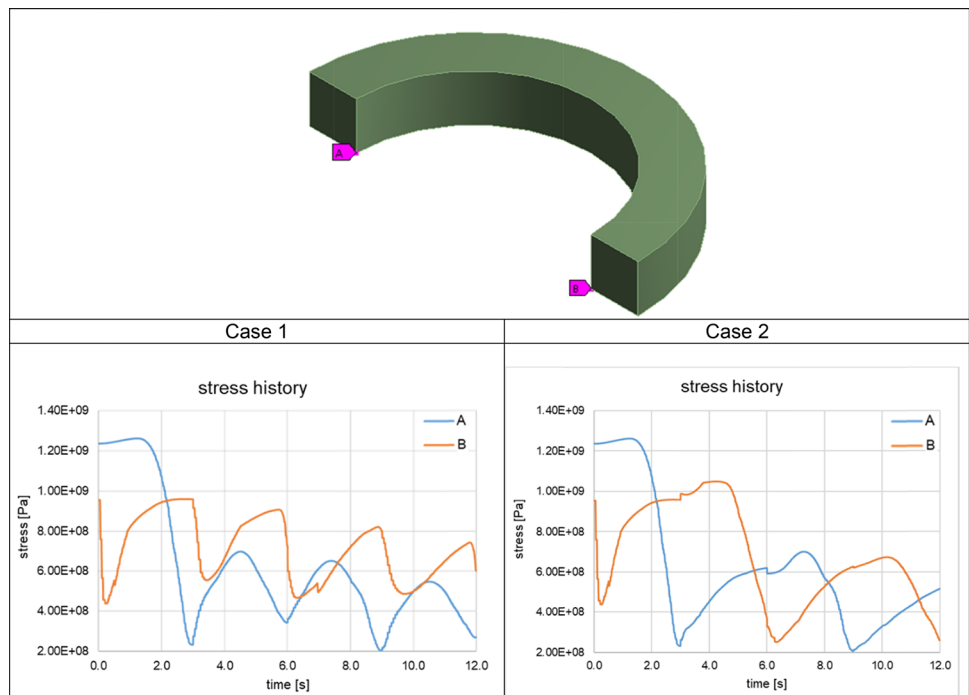


Fig. 18 Stress history: Points A, B, C, and D



4 Conclusions

The thermo-mechanical behavior of the additive manufacturing process is analyzed in the investigation using finite element analysis. The results of this investigation are first verified against published numerical results and excellent correlation was obtained. More complexity was added to the geometry in this study by simulating the building of a half cylinder as compared to the straight layers normally used in similar investigations. Using the developed computational model, the effect of varying the velocity direction on the 3D fields of temperature, strain, stress and deformation was investigated. In both tracking directions and due to the successive heating, the temperature of the deposited layers increased, which led to fewer thermal strains. The resulting thermal strains in Case 2 were slightly higher than those in Case 1 (CCW velocity direction). The locations of the maximum absolute values of the thermal strains depended on the depositing direction. In both studied cases, the deformation rose after the successive deposition of layers. However, in Case 1 the maximum deformations reached higher values than in Case 2 (alternating velocity direction). This could be due to the greater thermal gradient in Case 2. Moreover, the maximum deformations in Case 2 appeared in the middle of the deposited layers and not at the corner as in Case 1. High stresses appeared in the interface region of the substrate. These stresses reached their maximum value after the first layer, where the deformation was prevented, was deposited. This was owing to the colder body having a higher structural stiffness. The stresses decreased after further layers were deposited, and in Case 2, they were less concentrated than in Case 1. The maximum shear stress distributions were also analyzed in planes at different elevations and compared after each successive layer. The shear stress concentration positions depended on the direction of deposition and they followed the same trend observed in the thermal strain and the normal von Mises stress. Furthermore, carrying out the deposition process according to Case 1 led to higher shear stresses. The time history analysis of the stress at the interface points between the first layer and the substrate showed variations in the deposition along the depositing direction. The future work will extend the current work to include building more complex 3D models with a layer thickness of 0.1 mm which simulates the actual layer thickness in AM. In addition, different scan paths will be investigated to understand the thermal characteristics under varied scanning conditions. The thermal stresses and cooling rates will be co-related to the solidification kinetics and microstructure of the alloys obtained using experimental data. Using Artificial Intelligence/Machine Learning (AI/ML) methods it is possible to generate surrogate models that can predict microstructure evolution in real-time thus enhancing the quality of the printed components while reducing the failure rates.

Acknowledgements The authors acknowledge the support from NSERC-Canada. Argonne National Laboratory's work was supported in part by the U.S. Department of Energy Office of Science, under contract DE-AC02-06CH11357.

References

- Schmidt, M., Merklein, M., Bourell, D., Dimitrov, D., Hausotte, T., Wegener, K., Overmeyer, L., Vollertsen, F., Levy, G.: Laser based additive manufacturing in industry and academia. *CIRP Ann. Manuf. Technol.* **66**, 561–583 (2017)
- Khairallah, S.A., Anderson, A.T., Rubenchik, A., King, W.E.: Laser powder-bed fusion additive manufacturing: physics of complex melt flow and formation mechanisms of pores, spatter, and denudation zones. *Acta Mater.* **108**, 36–45 (2016)
- Tapia, G., Khairallah, S., Matthews, M., King, W.E., Elwany, A.: Gaussian process-based surrogate modeling framework for process planning in laser powder-bed fusion additive manufacturing of 316L stainless steel. *Int. J. Adv. Manuf. Technol.* **94**, 3591–3603 (2018)
- Wang, L., Felicelli, S., Gooroochurn, Y., Wang, P.T., Horstemeyer, M.F.: Optimization of the LENS process for steady molten pool size. *Mater. Sci. Eng. A (Struct. Mater. Prop. Microstruct. Process.)* **474**, 148–156 (2008)
- Karayagiz, K., Elwany, A., Tapia, G., Franco, B., Johnson, L., Ji, M.A., Karaman, I., Arróyave, R.: Numerical and experimental analysis of heat distribution in the laser powder bed fusion of Ti-6Al-4V. *IISE Trans.* **51**, 136–152 (2019)
- Zhao, X., Iyer, A., Promopattum, P., Yao, S.C.: Numerical modeling of the thermal behavior and residual stress in the direct metal laser sintering process of titanium alloy products. *Addit. Manuf.* **14**, 126–136 (2017)
- Khanafer, K., Al-Masri, A., Aithal, A., Deiab, I.: Multiphysics modeling and simulation of laser additive manufacturing process. *Int. J. Interact. Des. Manuf. (IJIDeM)* **13**, 537–544 (2019)
- Li, C., Liu, Z.Y., Fang, X.Y., Guo, Y.B.: Residual stress in metal additive manufacturing. *Proc. CIRP* **71**, 348–353 (2018). <https://doi.org/10.1016/j.procir.2018.05.039>
- Strantzla, M., Ganeriwala, R.K., Clausen, B., Phan, T.Q., Levine, L.E., Pagan, D., King, W.E., Hodge, N.E., Brown, D.W.: Coupled experimental and computational study of residual stresses in additively manufactured Ti-6Al-4V components. *Mater. Lett.* **231**, 221–224 (2018). <https://doi.org/10.1016/j.matlet.2018.07.141>
- Ali, H., Ma, L., Ghadbeigi, H., Mumtaz, K.: In-situ residual stress reduction, martensitic decomposition and mechanical properties enhancement through high temperature powder bed pre-heating of selective laser melted Ti6Al4V. *Mater. Sci. Eng. A* **695**, 211–220 (2017). <https://doi.org/10.1016/j.msea.2017.04.033>
- Wu, A.S., Brown, D.W., Kumar, M., Gallegos, G.F., King, W.E.: An experimental investigation into additive manufacturing-induced residual stresses in 316L stainless steel. *Metall. Mater. Trans. A* **45**, 1–11 (2014)
- Li, C., Liu, J.F., Guo, Y.B.: Prediction of residual stress and part distortion in selective laser melting. *Proc. CIRP* **45**, 171–174 (2016). <https://doi.org/10.1016/j.procir.2016.02.058>
- Conti, P., Cianetti, F., Pileri, P.: Parametric finite elements model of SLM additive manufacturing process. *Procedia Struct. Integr.* **8**, 410–421 (2018)
- Mukherjee, T., Zhang, W., Debroy, T.: An improved prediction of residual stresses and distortion in additive manufacturing. *Comput. Mater. Sci.* **126**, 360–372 (2017)

15. Yang, Q., Zhang, P., Cheng, L., Min, Z., Chyu, M., To, A.: Finite element modeling and validation of thermomechanical behavior of Ti-6Al-4V in directed energy deposition additive manufacturing. *Addit. Manuf.* **12**, 169–177 (2016)
16. Chiumenti, M., Cervera, M., Salmi, A., de Saracibar, C.A., Dialami, N., Matsui, K.: Finite element modeling of multi-pass welding and shaped metal deposition processes. *Comput. Methods Appl. Mech. Eng.* **199**, 2343–2359 (2010)
17. Bontha, S., Klingbeil, N.W., Kobryn, P.A., Fraser, H.L.: Thermal process maps for predicting solidification microstructure in laser fabrication of thin-wall structures. *J. Mater. Process. Technol.* **178**, 135–142 (2006)
18. Fachinotti, V.D., Cardona, A., Baufeld, B., van der Biest, O.: Finite-element modelling of heat transfer in shaped metal deposition and experimental validation. *Acta Mater.* **60**, 6621–6630 (2012)
19. Gan, Z., Liu, H., Li, S., He, X., Yu, G.: Modeling of thermal behavior and mass transport in multi-layer laser additive manufacturing of Ni-based alloy on cast iron. *Int. J. Heat Mass Transf.* **111**, 709–722 (2017)

Publisher's Note Springer Nature remains neutral with regard to jurisdictional claims in published maps and institutional affiliations.